Super-Resolution Fingerprinting Detects Chemical Reactions and Idiosyncrasies of Single DNA Pegboards

Alexander Johnson-Buck,[†] Jeanette Nangreave,[‡,§] Do-Nyun Kim,[‖] Mark Bathe,[‖] Hao Yan,[‡,§] and Nils G. Walter*,[†]

[†]Department of Chemistry, 930 N. University Avenue, University of Michigan, Ann Arbor, Michigan 48109-1055, United States
[‡]The Biodesign Institute and [§]Department of Chemistry and Biochemistry, Arizona State University, Tempe, Arizona 85287, United States
[‖]Department of Biological Engineering, Massachusetts Institute of Technology, Cambridge, Massachusetts 02139, United States

Ⓢ *Supporting Information*

ABSTRACT: We employ the single-particle fluorescence nanoscopy technique points accumulation for imaging in nanoscale topography (PAINT) using site-specific DNA probes to acquire two-dimensional density maps of specific features patterned on nanoscale DNA origami pegboards. We show that PAINT has a localization accuracy of ~10 nm that is sufficient to reliably distinguish dense ($>10^4$ features μm^{-2}) sub-100 nm patterns of oligonucleotide features. We employ two-color PAINT to follow enzyme-catalyzed modification of features on individual origami and to show that single nanopegboards exhibit stable, spatially heterogeneous probe-binding patterns, or "fingerprints." Finally, we present experimental and modeling evidence suggesting that these fingerprints may arise from feature spacing variations that locally modulate the probe binding kinetics. Our study highlights the power of fluorescence nanoscopy to perform quality control on individual soft nanodevices that interact with and position reagents in solution.

KEYWORDS: *Chemical imaging, DNA origami, PAINT, points accumulation for imaging in nanoscale topography, single molecule super-resolution fluorescence microscopy*
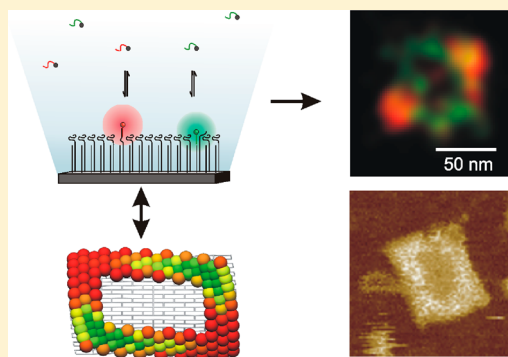
DNA nanotechnology[1−4] has laid the foundation for a multitude of nanoscale devices that permit control over dynamic chemical or optoelectronic processes.[5−10] Many of these devices are chemically heterogeneous and labile, incorporating flexible biological components that are often closely spaced. While techniques such as atomic force microscopy (AFM) and transmission electron microscopy (TEM) yield detailed topological maps of such devices, they can damage biological samples over time and possess limited chemical specificity. As a result, AFM and TEM provide incomplete information about compositionally complex and dynamic nanodevices. Alternatively, functional characterization of DNA-based nanoscale devices is often carried out in bulk,[6,8,9,11−13] potentially masking variations in performance between individual copies of a device or within different regions of a single device.

Nanoscale fluorescence microscopy (or short, nanoscopy[14−19]) has recently advanced to combine high spatial resolution and tunable chemical specificity with relatively low invasiveness and therefore holds promise for the spatiotemporal imaging and quality control of functional nanomaterials.[10,15,17,18,20,21] This body of techniques uses spatially confined illumination schemes[22,23] or repeated sparse sampling of features using single molecule emitters[14,24,25] to achieve resolutions well below the classical optical diffraction limit. It was recently shown that the super-resolution technique points accumulation for imaging in nanoscale topography (PAINT)[14] can be used to measure the position and hybridization kinetics of specific, spatially isolated features on DNA scaffolds.[15] In the present work, we show that PAINT can map the position and accessibility of specific single-stranded DNA (ssDNA) features in the context of very dense nanoscale arrays with spacings of only ~5 nm between adjacent features. We further use two-color PAINT to spatiotemporally monitor enzymatic modification of the ssDNA features, demonstrating the ability to visualize chemical changes on individual nanostructures. Finally, combining results from two-color PAINT with those from the finite-element model CanDo,[26] we present evidence that local variations in the DNA tile conformation and density of ssDNA features can result in spatially heterogeneous binding properties that would escape detection by other imaging techniques.

As targets for fluorescence nanoscopy, 60 × 90 nm rectangular DNA origami tiles[1] were synthesized, each bearing 42 or 126 identical single-stranded overhangs for the
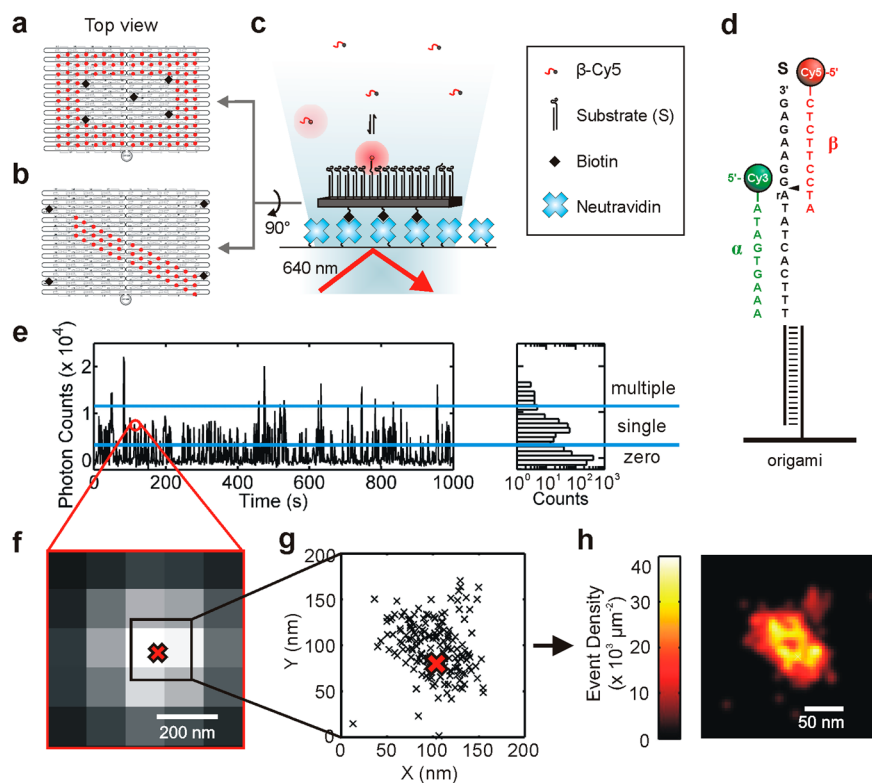
Figure 1. Origami tile designs used in this study: (a) rectangular origami R bearing 126 substrates (red circles) and 5 biotin molecules (black diamonds) for immobilization on a NeutrAvidin-coated microscope slide; and (b) linear origami L bearing 42 substrates and 4 biotin molecules. Substrates and biotins are displayed on opposite faces of the tile. (c) Scheme for PAINT experiments. DNA origami were immobilized on a NeutrAvidin-coated fused silica slide on a TIRF microscope via multiple biotin-NeutrAvidin interactions. Imaging occurred in the presence of single-stranded DNA probes that were fluorescently labeled at their 5′-end. As probes bind reversibly to the substrates on the origami tile, they enter the evanescent field of excitation light and are localized. (d) Sequences of the substrate (S) and fluorescently labeled PAINT probes α-Cy3 and β-Cy5. In some experiments, only β-Cy5 was used; in others, β was labeled with Cy3 and α was labeled with Cy5. S contains an RNA base (rA) to allow for enzymatic cleavage at the site indicated by the black triangle. (e) Fluorescence intensity time trace and histogram showing repeated binding of β-Cy5 to a single R origami tile. Only binding events with intensity between the two horizontal blue lines were used in the reconstruction, as these have a high probability of originating from individual β-Cy5 molecules (rather than ≥ 2 bound simultaneously). For ease of viewing, only 1000 s are shown from a 3000 s experiment. (f) Wide-field diffraction-limited fluorescence image of the β-Cy5 binding event circled in (e). The intensity profile is fit with a 2D Gaussian function to localize the binding event (red X). (g) Coordinates of 174 localizations of β-Cy5 binding PAINT reconstruction of an R origami. The red X corresponds to the localization of the binding event shown in (f). (h) PAINT reconstruction of the origami shown in (g). Each experiment yielded reconstructions for $\sim$20−100 origami.

attachment of substrate (S) oligonucleotides via a 20-base-pair DNA duplex (Figure 1a−d, Supporting Information Figure S1, Table S1). In addition, each tile had 4−5 overhangs bearing biotins on the face opposite to that of S for immobilization of the tiles in random orientations (Supporting Information Figure S2) on a NeutrAvidin-coated microscope slide (Figure 1c). Upon saturation with excess S (Supporting Information Figure S3), the tiles were immobilized on a microscope slide at a density of $\sim$0.1 μm^{-2} and imaged on a total internal reflection fluorescence (TIRF) microscope in the presence of one or two probe strands, α and/or β (Figure 1c,d, Supporting Information Figure S4). Each probe was labeled at its 5′-end with a fluorophore (Cy3 or Cy5) to permit its detection upon transient binding to the DNA origami within the evanescent field of excitation light. The concentration of probes was adjusted to an optimal range of 10−20 nM so that, in general, no more than one copy of each probe was bound to a given origami at a time (Figure 1e). This ensures accurate localization of individual binding sites, as opposed to averaged locations of multiple sites, and minimizes competition between probes (Figure 1d). We found that α and β dissociate from origami-

bound S with rate constants of 0.34 ± 0.01 and 0.22 ± 0.03 s^{-1}, respectively (Supporting Information Table S2).

In each experiment, the tiles were imaged for up to 66 min, yielding 20−300 binding events per tile. The fluorescence emission profile from each probe was fit with a 2D Gaussian function to localize the probe (Figure 1f). Intensity thresholding, aided by Hidden Markov modeling, was used to select intervals in which only one probe was bound (Figure 1e). Finally, a super-resolution reconstruction was generated in which each localization was represented as a Gaussian distribution with x and y standard deviations calculated based on photon count and other imaging parameters[27] with a typical value of $\sigma = 5−10$ nm. (We found it essential to correct for microscope stage drift and to account for the impact of sampling density on the reconstruction quality; see Supporting Methods, Figures S5−S6.) These reconstructions show a dramatic improvement in resolution over the corresponding diffraction-limited images (compare Figure 1f,h).

To examine the ability of PAINT to discern different spatial arrangements of the target, tiles bearing two patterns of S were synthesized: an open rectangle, R (Figure 1a), and a straight line, L (Figure 1b). Both patterns were imaged under identical
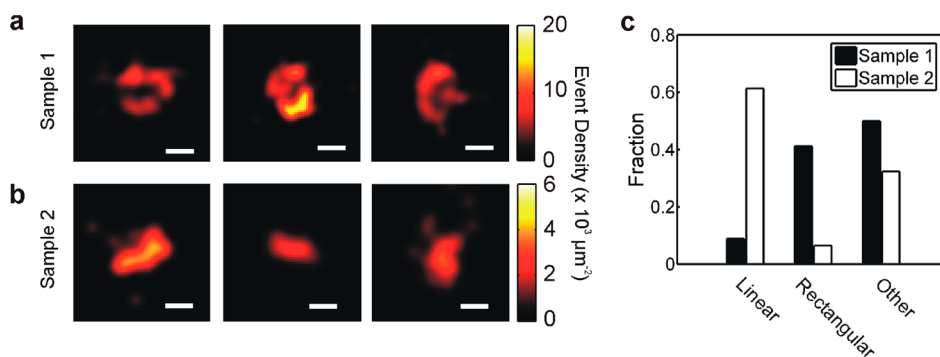
Figure 2. One-color PAINT reconstructions of R (a) and L (b) origami tiles imaged in the presence of 10 nM β-Cy5 with 20−60 binding events per tile. Scale bars: 50 nm. (c) Results from a blind experiment in which two origami samples of unknown identity (either L or R) were imaged in the presence of 10 nM β-Cy5 and classified according to their morphology: linear (e.g., panel b), rectangular (e.g., panel a), or other (42 and 27 origami were examined from samples 1 and 2, respectively). The "other" category likely included malformed origami tiles, aggregates of multiple origami, or origami with spatially heterogeneous binding of β-Cy5 (see Figure 4). Samples 1 and 2 were correctly identified as R and L, respectively.
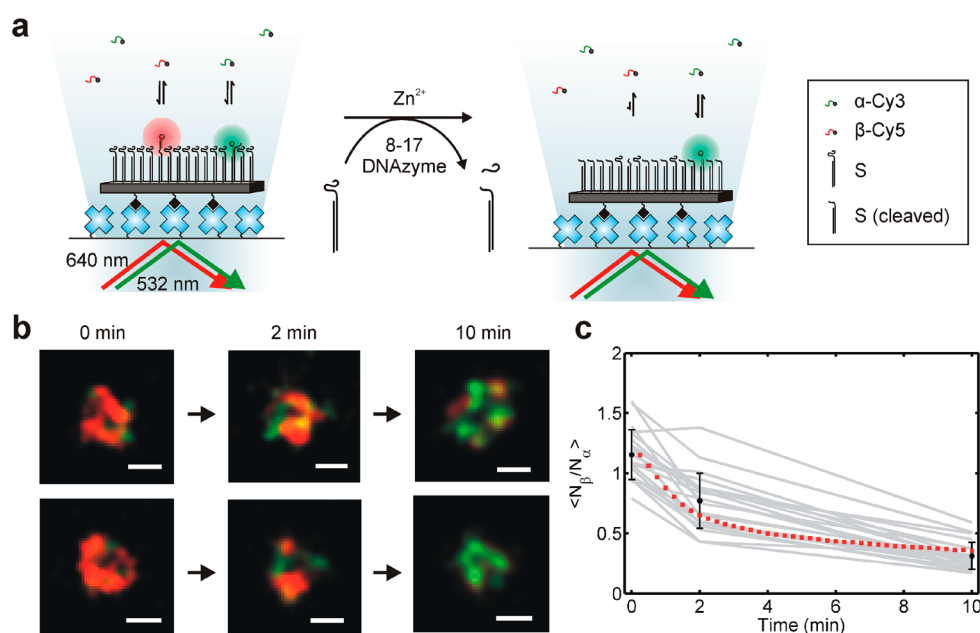

Figure 3. (a) Experiment for monitoring chemical changes by two-color PAINT. R origami tiles were imaged in the presence of 10 nM each of α-Cy3 and β-Cy5. Incubation with 1 μM 8−17 deoxyribozyme (DNAzyme) and 1 mM Zn^{2+} results in the cleavage of S. The cleavage product can bind probe α, but not probe β, resulting in a change in the PAINT readout. (b) Two-color reconstructions of three individual R origami tiles after 0, 2, or 10 min total incubation with 8−17 DNAzyme and Zn^{2+} (α-Cy3, green; β-Cy5, red, scale bars 50 nm). (c) Mean ratio of β binding events to α binding events for 21 R origami after 0, 2, or 10 min total incubation with 1 μM 8−17 DNAzyme and 1 mM ZnSO$_4$ (black circles, error bars 1 s.d.). The time courses for 21 individual origami tiles are also shown (gray lines). An ensemble time course for the cleavage of substrate on R origami under identical conditions, normalized to the initial value of $\langle N_\beta/N_\alpha \rangle$, is shown for comparison (red squares, Supporting Information Figure S3).

conditions, resulting in only a few dozen localizations per origami on average. Despite the sparse sampling (Supporting Information Figure S6a,b), the resulting PAINT reconstructions revealed binding patterns reflecting the design (Figure 2a-b) and permitted correct identification of R and L in a blind experiment (Figure 2c). For both patterns, a significant fraction (~33% for L, ~50% for R) of reconstructions could not be classified as linear or rectangular, which is in agreement with independent estimates of assembly yield from AFM images (Supporting Information Table S3). Furthermore, a model-free alignment of 198 reconstructions of R origami, each comprising a larger number of 100−300 localizations (Supporting Information Figure S7), using standard single particle analysis software EMAN revealed several class averages resembling the desired rectangular structure (45−55% of origami), with most

of the remaining class averages resembling aggregated or incompletely assembled origami. Many defects revealed in the PAINT images have counterparts in AFM images (Supporting Information Figure S7), suggesting that they are due to imperfect tile or pegboard assembly. This is consistent with the fact that the number of binding events per origami is distributed more broadly than would be predicted for binding to a set of identical, fully assembled pegboards (Supporting Information Figure S8). We note, however, that PAINT monitors the single-stranded DNA regions involved in interactions with external reagents that are too soft to be visible by AFM.

To demonstrate sequence-specific imaging, the R pattern was evaluated simultaneously in the presence of α-Cy3 and β-Cy5. The resulting binding patterns were reconstructed and
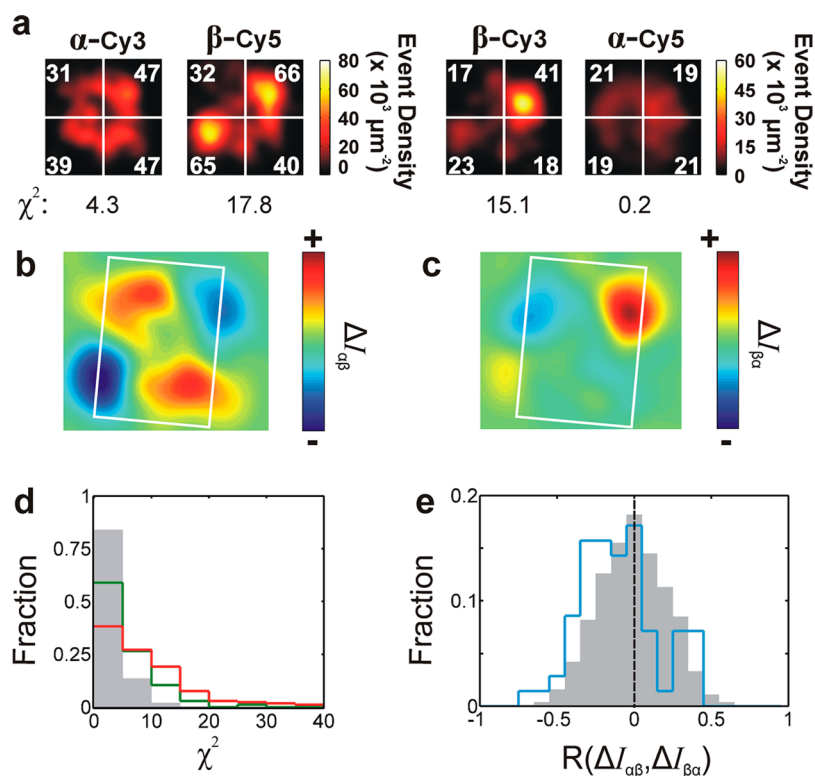
Figure 4. (a) DNA-PAINT reconstructions of the same R origami tile using two different sets of probes: α-Cy3 + β-Cy5, and β-Cy3 + α-Cy5, and quantification of binding uniformity by χ^2 analysis of the distribution of binding events between origami quadrants. The number of binding events observed in a 60 min period is indicated in each quadrant. The distributions of α-Cy3 and α-Cy5 binding can be explained by a homogeneous model, while that of β-Cy5 and β-Cy3 cannot (df = 3, $P < 0.001$). Reconstructions are 125×125 nm^2. (b,c) Intensity difference maps, calculated by subtracting the Cy5 reconstruction from the Cy3 reconstruction, for the origami tile shown in (a) as imaged by the two probe sets. White rectangular outlines depict typical origami dimensions as measured by AFM (60×90 nm). In (b), $\Delta I_{\alpha\beta} = I_{\alpha\text{-Cy3}} - I_{\beta\text{-Cy5}}$, while in (c), $\Delta I_{\beta\alpha} = I_{\beta\text{-Cy3}} - I_{\alpha\text{-Cy5}}$. The difference maps in (b) and (c) have a correlation coefficient $R = -0.67$. (d) Histograms of χ^2 for the binding distributions of probes α (green line) and β (red line) to 173 R origami, as compared to the distribution predicted from 1000 simulated R origami (gray shaded region). (e) Histogram of correlation coefficients between difference maps $\Delta I_{\alpha\beta}$ and $\Delta I_{\beta\alpha}$ for 70 R origami tiles (blue line; $\mu = -0.10$, standard error of the mean (s.e.m.) = 0.03) as compared to the results from 1000 simulated tiles (gray shaded region; $\mu = -0.008$, s.e.m. = 0.008). The black dashed line indicates the mean value of the simulated distribution. The experimental distribution is significantly skewed toward negative values compared to the simulated distribution ($t(69) = 3.1$, two-tailed $P = 0.003$).

registered in the same coordinate space, resulting in a two-color overlay (Figure 3b, Supporting Information Figure S9). Unlike other fluorescence nanoscopy techniques, PAINT is insensitive to photobleaching and labeling efficiency due to the vast reserve of probes in solution that are readily exchanged for origami-bound probes, enabling stable imaging over hours. Since S contains a single ribonucleotide (Figure 1d), it can be site-specifically cleaved by an 8−17 DNAzyme in the presence of Zn^{2+} such that, after cleavage, the β-Cy5 binding frequency is expected to diminish relative to that of α-Cy3. Incubation with the deoxyribozyme results in a time-dependent decrease in β-Cy5 relative to α-Cy3 binding, consistent with but going beyond ensemble-averaged measurements (Figure 3b,c, Supporting Information Figure S3) by demonstrating PAINT's ability to spatiotemporally monitor enzymatic remodeling reactions on individual origami nanodevices.

The use of two probe strands also provides a means of assessing the homogeneity of binding to nanostructures. Surprisingly, we found several cases where one probe bound uniformly across the pattern of S and the other did not, even for well-formed R patterns (Figure 4a). To rule out fluorophore-specific imaging errors as the source of nonuniform binding, a set of R origami was imaged first with the probe combination α-Cy3 + β-Cy5 and subsequently with the labels inverted, that is,

β-Cy3 + α-Cy5. A χ^2 test of homogeneity across different quadrants of the rectangular pattern (Supporting Information Figure S9) revealed that the binding patterns of α-Cy3 and α-Cy5 to the origami in Figure 3 are indistinguishable from homogeneous binding, while the binding of β-Cy5 and β-Cy3 cannot be explained by a homogeneous model ($\chi^2(3, N > 99) > 15$, $P < 0.002$). Furthermore, the intensity difference profile, calculated by subtracting the Cy5 reconstruction from the Cy3 reconstruction (Supporting Information Figure S10), appears to invert upon switching the probe labels (Figure 3b,c), with a two-dimensional (2D) correlation coefficient of -0.67. Taken together, these observations suggest a "fingerprint" of sequence-specific binding patterns for this tile with more heterogeneous binding of β than α, and that this fingerprint persists throughout the ~1 h time lag between imaging with α-Cy3 + β-Cy5 and β-Cy3 + α-Cy5.

To determine how prevalent heterogeneous binding is within a population of R origami, we compared the observed distribution of χ^2 for 173 origami to the theoretical distribution from 1000 simulated origami (Figure 4d). For both α and β, χ^2 is skewed toward larger values than predicted from homogeneous binding, which is consistent with the observed incomplete and variable assembly of a significant fraction of the S patterns as noted in the yield estimates by AFM (Supporting
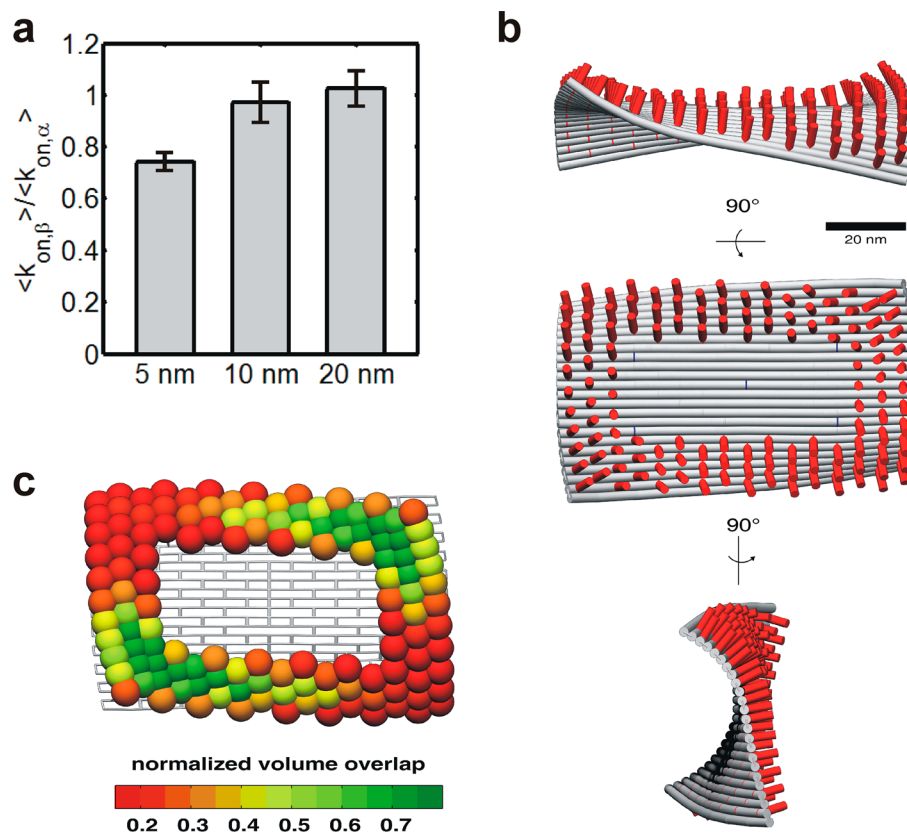
Figure 5. (a) Relative association rate constants of α-Cy3 and β-Cy5 to origami with approximate distances of 5, 10, or 20 nm between adjacent S strands. Error bars: 1 s.e.m. (b) Three-dimensional solution structure of R origami tile predicted by CanDo with constrained biotin positions (see Supporting Information). Red cylinders represent S positions. (c) Normalized effective volume overlap of neighboring free S strands on R origami based on the CanDo structural model in panel (b).

Information Table S3 and Figure S11). However, the binding of β is more heterogeneous than that of α, a fact that cannot be explained by assembly yield alone and is not detectable by AFM imaging. To further characterize the sequence dependence and stability of binding distributions, the 2D correlation coefficient between difference profiles with the two inversely labeled sets of PAINT probes (as in Figure 4b,c) was calculated for 70 origami and compared to the values expected from 1000 simulated origami (Figure 4e). The distributions are broadened by limited sampling, but there is a bias toward negative correlation coefficients in the experimental set, indicating a sequence-specific heterogeneity of binding that persists for at least 1 h. Importantly, these patterns cannot be trivially attributed to a fraction of precleaved S, which would lack the β-binding sequence (Supporting Information Figure S12). Furthermore, binding heterogeneity is not significantly correlated with the total number of binding events (Supporting Information Figure S8), which implies that some well-assembled origami with intact S nevertheless bind probes unevenly. Together, these data suggest that the accessibility of β-binding sequence varies across the surface of the origami largely independent of the accessibility of α-binding sequence.

We therefore hypothesized that local interactions between adjacent S strands exert a differential influence on α and β binding. To test this possibility, we measured the kinetics of α-Cy3 and β-Cy5 binding to origami with spacings of ∼5, 10, or 20 nm between nearest-neighbor S strands (Supporting Information Figure S13). We found that β-Cy5 binding is slowed by ∼25% relative to that of α-Cy3 at a spacing of 5 nm

between S strands but not 10 or 20 nm (Figure 5a). This is consistent with a model in which interactions between nearby S strands compete with β binding, inhibiting rather than enhancing its binding relative to α (Supporting Information Figure S14). Thus, if the spacing of S varies across the surface of a tile, there may be regions in which β-Cy5 binding is inhibited relative to that of α-Cy3, resulting in heterogeneous binding fingerprints such as those in Figure 4.

A variety of factors could produce variation in S spacing across the surface of an origami array, including global bend/twist or distortion of the origami tile[26,28,29] and incomplete tile or staple assembly. To investigate the possible impact of tile distortion on S spacing, we used the finite-element model CanDo (see Supporting Information) to predict the three-dimensional solution conformation of the R origami tile, accounting for constraints imposed by surface immobilization via biotin. The model predicts a saddlelike conformation with significant curvature (Figure 5b, Supporting Information Figure S15), consistent with previous reports.[26,28,29] Using a simple model of free S as a flexible, freely jointed chain with root-mean-square end-to-end distance of 3.6 nm connected to the origami surface by a rigid double-stranded DNA rod of ∼7 nm length (see Supporting Information Figure S16), the effective local concentration of S is predicted to vary 2- to 4-fold between different corners of the tile (Figure 5c, Supporting Information Figure S16). These predictions are consistent with binding patterns observed in PAINT reconstructions (Supporting Information Figure S17) and a competitive inhibition model in which nearest-neighbor strands interact via non-

canonical or nonspecific binding interactions that are enhanced or diminished by structurally induced changes in interstrand proximity. Relaxation of the position restraints at the biotin positions predicts less pronounced curvature at the corners (Supporting Information Figure S15b) and consequently less variation in S concentration across the tile (Supporting Information Figure S16c), suggesting that the number and orientation of surface-bound biotins can influence local variations in S spacing. Furthermore, since both PAINT (Supporting Information Figure S8) and AFM (Supporting Information Figure S11, Table S3) images show evidence of incomplete tile assembly, it is also possible that variations in assembly play a role in generating the fingerprints observed (Supporting Information Figure S10), as structural defects could also generate local variations in spacing between S strands.

Previous studies have presented mixed evidence for spatially dependent oligonucleotide binding to origami with a slight (10−40%) preference for binding toward the outer edges.[4,15] Our findings further show that individual origami tiles bearing dense arrays of targets can have stable fingerprints of sequence-specific interactions with binding kinetics varying as much as 2-fold between different corners or edges of the tile (Figure 4 b,c,e). S has little self-complementarity (Figure 1d), but the locally high concentration (~2−8 mM by our model) of S may lead to non-Watson−Crick interactions such as G-tetrads[30] between neighboring S strands that, even if transient, may compete with probe binding in a sequence-specific fashion.

In summary, we employed multicolor PAINT to acquire detailed 2D maps of chemical properties of individual DNA origami tiles, revealing their previously unobservable, stable, idiosyncratic fingerprints of interaction with reagents in solution. In addition, we have shown that the low invasiveness and insensitivity to photobleaching make PAINT suitable for spatiotemporal monitoring of subtle chemical modifications to individual nanostructures. Since it reveals previously hidden properties of nonrigid features of DNA origami that can be functionalized but yield little contrast for AFM and electron microscopy, PAINT complements these more established analytical tools. PAINT should thus find broad application in the characterization of the growing toolkit of soft, internally complex, nanoscale devices with applications in fields as diverse as organic synthesis, optoelectronics, and molecular robotics.[10,31,32]

■ ASSOCIATED CONTENT

Ⓢ Supporting Information

Materials and Methods; Figures S1−S17; Tables S1−S3. This material is available free of charge via the Internet at http://pubs.acs.org.

■ AUTHOR INFORMATION

Corresponding Author
*E-mail: nwalter@umich.edu.

Notes
The authors declare no competing financial interest.

■ ACKNOWLEDGMENTS

■ REFERENCES

(1) Rothemund, P. W. K. *Nature* **2006**, *440*, 297−302.

(2) Han, D.; Pal, S.; Nangreave, J.; Deng, Z.; Liu, Y.; Yan, H. *Science* **2011**, *332*, 342−346.

(3) Pinheiro, A. V.; Han, D.; Shih, W. M.; Yan, H. *Nat. Nanotechnol.* **2011**, *6*, 763−772.

(4) Ke, Y.; Lindsay, S.; Chang, Y.; Liu, Y.; Yan, H. *Science* **2008**, *319*, 180−183.

(5) Gu, H.; Chao, J.; Xiao, S.-J.; Seeman, N. C. *Nature* **2010**, *465*, 202−205.

(6) He, Y.; Liu, D. R. *Nat. Nanotechnol.* **2010**, *5*, 778−782.

(7) Maune, H. T.; Han, S.; Barish, R. D.; Bockrath, M.; Iii, W. A. G.; Rothemund, P. W. K.; Winfree, E. *Nat. Nanotechnol.* **2009**, *5*, 61−66.

(8) Douglas, S. M.; Bachelet, I.; Church, G. M. *Science* **2012**, *335*, 831−834.

(9) Kuzyk, A.; Schreiber, R.; Fan, Z.; Pardatscher, G.; Roller, E.-M.; Högele, A.; Simmel, F. C.; Govorov, A. O.; Liedl, T. *Nature* **2012**, *483*, 311−314.

(10) Lund, K.; Manzo, A. J.; Dabby, N.; Michelotti, N.; Johnson-Buck, A.; Nangreave, J.; Taylor, S.; Pei, R.; Stojanovic, M. N.; Walter, N. G.; Winfree, E.; Yan, H. *Nature* **2010**, *465*, 206−210.

(11) Tian, Y.; He, Y.; Chen, Y.; Yin, P.; Mao, C. *Angew. Chem., Int. Ed.* **2005**, *44*, 4355−4358.

(12) Wickham, S. F. J.; Bath, J.; Katsuda, Y.; Endo, M.; Hidaka, K.; Sugiyama, H.; Turberfield, A. J. *Nat. Nanotechnol.* **2012**, *7*, 169−173.

(13) Fu, J.; Liu, M.; Liu, Y.; Woodbury, N. W.; Yan, H. *J. Am. Chem. Soc.* **2012**, *134*, 5516−5519.

(14) Sharonov, A.; Hochstrasser, R. M. *Proc. Natl. Acad. Sci. U.S.A.* **2006**, *103*, 18911−18916.

(15) Jungmann, R.; Steinhauer, C.; Scheible, M.; Kuzyk, A.; Tinnefeld, P.; Simmel, F. C. *Nano Lett.* **2010**, *10*, 4756−4761.

(16) Walter, N. G.; Huang, C.-Y.; Manzo, A. J.; Sobhy, M. A. *Nat. Methods* **2008**, *5*, 475−489.

(17) Zhou, X.; Andoy, N. M.; Liu, G.; Choudhary, E.; Han, K.-S.; Shen, H.; Chen, P. *Nat. Nanotechnol.* **2012**, *7*, 237−241.

(18) Cang, H.; Labno, A.; Lu, C.; Yin, X.; Liu, M.; Gladden, C.; Liu, Y.; Zhang, X. *Nature* **2011**, *469*, 385−388.

(19) Huang, B.; Babcock, H.; Zhuang, X. *Cell* **2010**, *143*, 1047−1058.

(20) Zürner, A.; Kirstein, J.; Döblinger, M.; Bräuchle, C.; Bein, T. *Nature* **2007**, *450*, 705−708.

(21) Kirstein, J.; Platschek, B.; Jung, C.; Brown, R.; Bein, T.; Bräuchle, C. *Nat. Mater.* **2007**, *6*, 303−310.

(22) Hell, S. W.; Wichmann, J. *Opt. Lett.* **1994**, *19*, 780−782.

(23) Gustafsson, M. G. L. *J. Microsc.* **2000**, *198*, 82−87.

(24) Rust, M. J.; Bates, M.; Zhuang, X. *Nat. Methods* **2006**, *3*, 793−796.

(25) Hess, S. T.; Girirajan, T. P. K.; Mason, M. D. *Biophys. J.* **2006**, *91*, 4258−4272.

(26) Kim, D.-N.; Kilchherr, F.; Dietz, H.; Bathe, M. *Nucleic Acids Res.* **2012**, *40*, 2862−2868.

(27) Thompson, R. E.; Larson, D. R.; Webb, W. W. *Biophys. J.* **2002**, *82*, 2775−2783.

(28) Li, Z.; Liu, M.; Wang, L.; Nangreave, J.; Yan, H.; Liu, Y. *J. Am. Chem. Soc.* **2010**, *132*, 13545−13552.

(29) Li, Z.; Wang, L.; Yan, H.; Liu, Y. *Langmuir* **2011**, *28*, 1959−1965.

(30) Burge, S.; Parkinson, G. N.; Hazel, P.; Todd, A. K.; Neidle, S. *Nucleic Acids Res.* **2006**, *34*, 5402−5415.

(31) Michelotti, N.; Johnson-Buck, A.; Manzo, A. J.; Walter, N. G. *Wiley Interdiscip. Rev.: Nanomed. Nanobiotechnol.* **2012**, *4*, 139−152.

(32) Nangreave, J.; Han, D.; Liu, Y.; Yan, H. *Curr. Opin. Chem. Biol.* **2010**, *14*, 608−615.